Journal of Applied Fluid Mechanics, Vol. 18, No. 6, pp. 1652-1668, 2025.
Available online at www.jafmonline.net, ISSN 1735-3572, EISSN 1735-3645.
https://doi.org/10.47176/jafm.18.6.3000

Study and Evaluation of the Effects of Bionic Groove Structures Applied to Wheel Spokes on the Aerodynamics of a Car Model

T. H. Huang[1†], H. C. Zhou[1], J. Yang[1], W. Zhang[1] and Q. Y. Chen[2]

[1] *School of Automotive and Traffic Engineering, Jiangsu University, Zhenjiang 212013, China*
[2] *China Automotive Engineering Research Institute Co. Ltd, Chongqing 401122, China*

†*Corresponding Author Email: 2222204152@stmail.ujs.edu.cn*

ABSTRACT

Decreasing the wheel aerodynamic drag is one of the important measures for lowering vehicle drag and improving fuel efficiency. The innovation of this study is designing the bionic non-smooth groove structure on the spoke surface as a drag reduction method and introducing the energy gradient function *K* value to characterize the aerodynamic drag. Wheels with and without grooved spoke structures were mounted on the Ahmed body, and the flow characteristics around the wheel region and car model were numerically investigated. A comparison between the numerical and experimental pressure distribution results was used to verify the accuracy of the numerical method. The numerical results demonstrated that the spoke designed with groove structures could reduce the aerodynamic drag of the car model and the wheels. Among the three groove structures studied, Case 1 (the forward groove structure) exhibited the greatest impact on drag decrease, with a reduction in the vehicle drag coefficient by 2.85%, the front wheels drag coefficient by 8.37%, and the rear wheels drag coefficient by 7.93%. The *Q* criterion was used to analyze the vortex flow around the wheels, and this analysis revealed that the designed groove structures reduced vortex generation, resulting in delayed flow separation and weakened energy dissipation, which decreased aerodynamic drag. Finally, the calculated K values suggested that the designed groove structures improved flow stability around the wheels, and the vehicle drag coefficient was positively correlated with K in the unstable-flow regions of the front and rear wheels.

Article History

Received July 22, 2024
Revised December 21, 2024
Accepted January 3, 2025
Available online March 30, 2025

Keywords:

Aerodynamic drag
Non-smooth structures
Large-eddy simulation
Ahmed model
Energy gradient theory

1. INTRODUCTION

Increasing vehicle ownership over time has contributed to a global energy crisis and increased greenhouse gas emissions. According to statistics from public security authorities, motor vehicle ownership worldwide reached 1300 million units in 2022, which greatly influences greenhouse gas emissions. Vehicle energy consumption continues to increase, and consumers and the government require more fuel efficiency. As a result, numerous present and scheduled laws are implemented to lower the energy usage of vehicles. Aerodynamic drag is positively related to the square of vehicle speed and is the main resistance source when cars travel at high speeds (Nath et al., 2021). When a car travels at 60 km/h or above, the power required to overcome aerodynamic drag accounts for half the total power required to overcome driving resistance (Wager et al., 2016). After the speed exceeds 80 km/h, roughly 75–80% of the driving resistance comes from aerodynamic drag (Zhou et al., 2022, 2024). Therefore, reducing aerodynamic drag can increase range and fuel economy, thus making cars greener.

In the past decade, scholars have conducted extensive research on low-drag vehicles, developing technologies for reducing aerodynamic drag. Among the most extensively investigated generic vehicle bodies is the Ahmed body (Ahmed et al., 1984), and many experimental and numerical studies have provided comprehensive insights into its flow characteristics and drag mechanism (Chok et al., 1994; Koppa Shivanna et al., 2021). Beaudoin and Aider (2008) found that the drag magnitude is closely related to the wake structure and also pointed out that the separation region generated at the vehicle's rear contributes significantly to the pressure difference resistance. Through experiments and simulations, the aforementioned researchers investigated techniques for controlling flow around the tail of an Ahmed body, minimizing drag, and managing the flow

NOMENCLATURE

f_i	particle distribution function	e_i	discrete velocity
Ω_i	collision operator	v_t	turbulent eddy viscosity
$S_{\alpha\beta}$	strain rate tensor of the resolved scales	$G^d_{\alpha\beta}$	strain rate tensor of the resolved scales
C_D	drag coefficient	C_P	coefficient of pressure
U	coefficient of slipstream speed	u_l	spatial velocity coefficient
F_D	aerodynamic drag	P	time-averaged hydrostatic pressure
P_0	reference pressure	U_f	inlet wind speed
U_x	wind speeds in the *X*-direction	U_z	wind speeds in the *Z*-direction
U_{local}	wind speed around the model	ρ	air density
Q	*Q* criteria	S_{ij}	symmetric parts of the velocity gradient tensor
Ω_{ij}	anti-symmetric parts of the velocity gradient tensor	K	energy gradient parameter
u	fluid velocity along the X-axis	v	fluid velocity along the Y-axis
w	fluid velocity along the Z-axis	μ_t	turbulent viscosity

field. They also employed passive and active control techniques to reduce drag and reported some positive findings. Beaudoin and Aider (2008) investigated the effects of installing plates with different configurations and installation angles on each side of the 30°Ahmed model rear. Their results indicated that placing plates on both sides of the rear slope suppressed the separation at the C-pillar and decreased the drag by 17.7%. Moreover, the installation of plates on all sides of the rear end reduced the drag by 25.2%. Phan et al. (2022) applied three flow control strategies to the Ahmed model's back edges for the back edges of the Ahmed model to reduce aerodynamic drag. Their results indicated that among the three adopted strategies, the strategy involving the use of a blowing jet produced the largest drag reduction. Khalighi et al. (2001) studied the flow structures in the transient wake of a plate-shaped drag reduction device-equipped bluff body. Behind the test model, they successfully altered the flow field, resulting in a change in the structure of the wake and a reduction in aerodynamic drag by over 20%.

However, functional requirements have limited the optimization of vehicle shapes, and the improvement in aerodynamic drag reduction through the optimization of overall vehicle shape has reached a technical bottleneck with limited potential for significant advancements (Klingbeil et al., 2016; Wang et al., 2017a; Wolf, 2020; Su et al., 2023). Notably, the aerodynamic drag generated by the vehicle body accounts for less than 50% of the overall aerodynamic resistance. Furthermore, the wheel area contributes one-fourth of the total aerodynamic drag (Wickern et al., 1997; Jermy et al., 2008; Josefsson et al., 2022). Studies have indicated that a vehicle's tyre, wheel rim, and wheel well areas account for approximately 25% of the total vehicle aerodynamic drag (Brandt et al., 2019). Studying the flow characteristics of the wheel area under rotating conditions and proposing drag reduction methods for the wheel area is of great significance in reducing automobile aerodynamic drag and fuel consumption. Hucho (2013) demonstrated that rotating wheels generate lower aerodynamic drag than stationary wheels. Moreover, Gleason et al., (2015) indicated that wheel spoke design can affect the flow division and features of the flow around the wheel area, leading to changes in vortex shedding at the tyre edge and altering the wheels' aerodynamic drag. In addition to investigating the aerodynamic drag mechanism and flow properties of the wheel region, both domestic and international researchers optimized the wheel configuration's structural parameters for controlling flow and achieving drag reduction, thereby enhancing vehicles' aerodynamic performance. Blacha and Islam (2017) conducted wind tunnel tests on an Audi Q5 and found that smooth transitions of the tyre sidewalls can reduce flow separation and decrease the vehicle drag coefficient. Bolzon et al., (2019) clarified the influence of wheel rim coverage area, fan spokes, and spoke sharpness on the passenger vehicle drag coefficient. They concluded that reducing the rim coverage area increased the drag coefficient, and rounding the spoke edges reduced the drag coefficient of a rotating wheel. Therefore, to reduce vehicle aerodynamic drag, the present study investigated the effects of non-smooth wheel spoke surface designs on the aerodynamic characteristics of a generic vehicle model, namely the Ahmed model.

Current drag reduction methods are passive or active. Research has indicated that non-smooth surfaces based on biomimetic design can influence the flow field structure near the wall, impede the development of turbulent boundary layers, reduce turbulence intensity, and minimize energy losses, thereby reducing drag. The main non-smooth surfaces used for drag reduction are groove, cavity, and adaptive surfaces; these surfaces offer unique advantages and engineering value. Viswanath (2002) studied the influence of the groove surfaces on high Reynolds-number conditions at different Mach numbers and achieved drag reduction effects of 5% to 8%. Rong and Yiwan (2019) arranged non-smooth riblet surfaces with triangular, circular, and rectangular shapes at the tail of the MIRA vehicle model. The drag reduction effects of all three types of non-smooth surfaces were favourable, with the circular non-smooth surface achieving the greatest reduction at 5.53%. Yang et al., (2016) placed concave-convex non-smooth surfaces at the tail of the MIRA bluff body model and reduced aerodynamic drag by altering the flow state of the near-wall airflow. Moreover, Wang et al., (2017b) explored the drag reduction effect of a non-smooth dimpled surface for a general vehicle. They found that the optimal dimpled structure resulted in a 5.2% lower aerodynamic drag coefficient.

For a more effective reduction of electric vehicle aerodynamic drag, wheel spokes with non-smooth surfaces have been used in some existing vehicle models, as shown in Fig. 1. Additionally, under the premise of

ensuring that the open area of a single spoke remains unchanged, Jiao et al., (2023) set up seven surface structures for the spokes of a certain type of wheel while ensuring that the open area of each spoke remained unchanged. The findings revealed that straight grooves on the spoke improved the aerodynamic characteristics of the wheel, reducing the aerodynamic drag coefficient by 4.1%, and the grooves were rounded on both spoke sides so that a part of the airflow was dispersed outward at the grooves, reducing the aerodynamic drag coefficient of the wheel by 2.4%. Besides, the research results of Zhou et al., (2015) showed that tread groove surfaces with non-smooth structures can improve tire anti-hydroplaning performance. The aforementioned non-smooth surface designs can reduce aerodynamic drag while meeting requirements for wheel stiffness and brake cooling.

Although the non-smooth structural design has been successfully applied in transportation and shipping fields, such as aircraft, high-speed trains, and automobiles, in vehicle aerodynamics research, the non-smooth design is mostly applied to bodywork surfaces or tyre surfaces to achieve vehicle drag reduction. Gao et al., (2024) studied the impact on the shape, arrangement, layout position, and size of non-smooth cells for vehicle aerodynamic characteristics based on the MIRA square back model. For the wheel region, Josefsson et al., (2022) analyzed and compared the effect of different groove forms set on the tyres on the aerodynamic resistance of the vehicle. The research on the non-smooth design of wheel spokes is still limited, and the mechanisms for the influence of non-smooth design on wheel aerodynamic drag also need to be further explored. Consequently, in this paper, the groove structure is applied to the wheel spoke surface, and the flow field differences are analyzed using the energy gradient theory. The rest of this paper is structured as follows. Section 2 elucidates the geometric model used in this study and the adopted pressure measurement method. Section 3 details the simulations conducted in this study. Section 4 describes the design of the grooved spoke surfaces and the verification of the numerical calculation method. Section 5 reports the results and discussions, including those related to the effects of different types of grooved spokes on the wheel drag coefficient and considered car model, the features of the flow field surrounding the car model, and the analysis of variations in the unstable flow region of the wheel from an energy perspective. Finally, Section 6 provides concluding remarks.

2. WIND TUNNEL TEST

2.1 Geometry Model

The classical Ahmed model with a rear angle of 35° was selected as the geometric model in this study. The essential features of the wheels and wheel housing shape were consistent with the physical vehicle equipped with a 255/35 R19 tyre (Ahmed et al., 1984). According to the work and experimental conditions of Huminic and Huminic (2017), a 1:2 scale test model was established in this study, wherein the wheel model was the small wheel of the luggage cart in daily life, all the detail sizes of the model are presented in Fig. 2.

(a) Lynk & Co 08 (b) BYD-Song DMI

(c) Audi-RS7 (d) Audi Q4 e-tron

Fig. 1 Non-smooth spoke structures in daily life

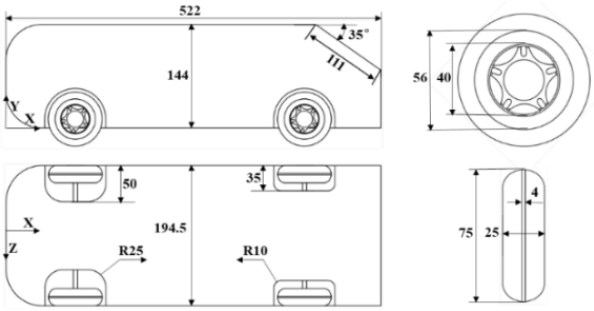

Fig. 2 Dimensions of the experimental car model (unit: mm)

2.2 Pressure Measurements

Considering the strength and quality of the body model, 3D shell extraction printing was carried out with resin material, and the wall thickness of the model was 3mm. As displayed in Fig. 3, the model was printed in two parts to facilitate the connection of pressure measurement pipes and silicone hoses. There were 59 pressure measuring points discretely scattered around the model tail, among which 32 and 27 were on the slant and the rear, respectively.

The different test points for the surface pressure of the model were conducted using electrical pressure transducer, the diameter of the test hole was 1 mm. Figure 4(a) displays the attachment of numbered silicone hoses to the experimental model. These silicone hoses were used to connect the electrical pressure transducer and the pressure test. The connection device is shown in Fig. 4.

Wind tunnel tests were conducted in the low-speed zone of the wind tunnel laboratory of Yangzhou University (Yangzhou, Jiangsu, China). This zone has a length, width, and height of 7, 3, and 3 m, respectively. As depicted in Fig. 5(a), the experimental model was fixed on the low-speed test bench, and the wheel of the model was driven by a miniature DC motor. In order to reduce the influence of the ground boundary layer and the platform device on the measurement results, a plastic plate was

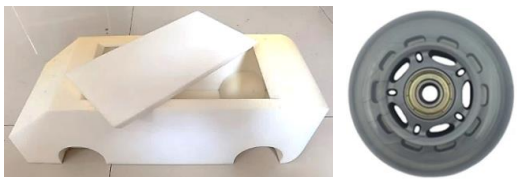

(a) Physical model

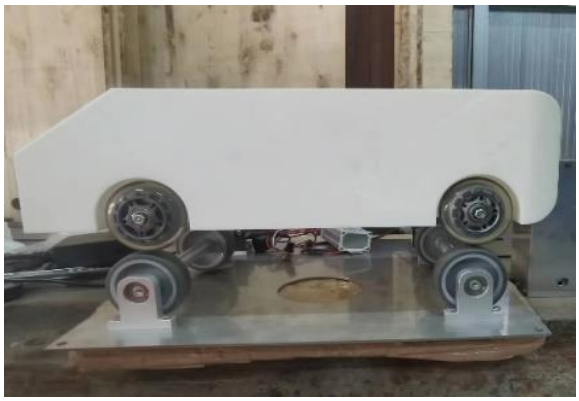

(b) Wheel rotation device

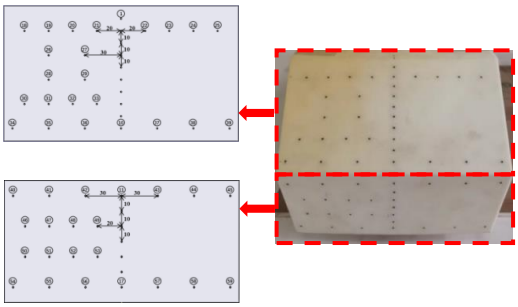

(c) Distribution of pressure points on the tail surface: the slant and the rear

Fig. 3 Experimental model, device and pressure point distribution

(a) Numbered silicone hose

(b) Pressure transducer

Fig. 4 Pressure measurement equipment

(a) Test model installed in the wind tunnel

(b) digital hand-held tachometer HT-4200 and wheel speed adjustment

Fig. 5 Wind tunnel install and test

added around the platform to extend the length and width of the upper surface of the platform to ensure no gap between the upper surface of the platform and the plate. Moreover, the hot wire anemometer system was used to measure and calibrate the airspeed.

According to the test wind speed, the corresponding speed of the model wheel was calculated, and the speed of the motor was adjusted to change the speed of the model wheel. In the test procedure, the wheel speed was measured using a high-performance and easy-to-operate digital hand-held tachometer HT-4200, as shown in the left panel of Fig. 5(b). This tachometer displays 30-50000 r/min with high precision and measures accurately 1 r/min in the speed range of 30-12500 r/min. The right panel of Fig. 5(b) illustrates the adjustment of the wheel speed.

3. NUMERICAL DETAILS

3.1 Computation of Domain and Boundary Conditions

As shown in Fig. 6, the computational domain had a length, width, and height of 7, 3, and 3 m, respectively; these dimensions are the same as those of the low-speed zone of the wind tunnel laboratory of Yangzhou University. The cross-section area was 3 m × 3 m, and the test model's projection area was S = 0.0288 m^2; thus, it provided a blockage ratio in the numerical wind tunnel of 0.32%, which satisfied computational requirements. The simulated car model was positioned 4.48 m from the outlet boundary and 2 m from the inlet boundary; the distance between both sides and the test model centre was 1.5 m. The initial airflow temperature for the virtual wind tunnel test was T = 293.15/(K), the density ρ was 1.225 kg/m^3, the pressure P was 1.013 × 10^5 Pa, and the kinetic viscosity coefficient was 1.81 × 10^{-5} Pa·s.

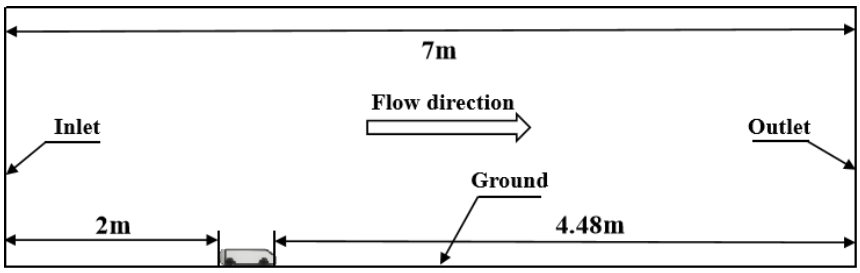

(a) Front view

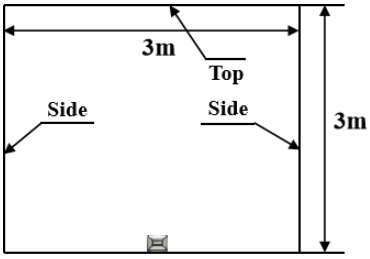

(b) Side view

Fig. 6 Dimensions of the computational domain and boundary conditions

The inlet was set as the uniform velocity inlet boundary condition with 10 m/s, and the pressure outlet boundary condition was applied to the corresponding outlet boundary, with a reference pressure of 0 Pa (the two walls vertical to the X-axis). The symmetry conditions were adopted on two lateral sides (the two walls vertical to the Z-axis). The top of the computational domain was set as the symmetry conditions, and the boundary condition of the free-slip wall was set on the ground, moving at the same speed of 10 m/s. All surfaces of the simulated model were considered to be no-slip wall boundaries. Wheel rotation was modeled using the Eulerian angle motion type for the stipulated rotary movement around the global coordinate axis. The wheel was set as the rotating movement around the Z-axis, and the rotation velocity was defined at X = 0, Y = 0, and Z = 360 n/t, t denotes the computation time, n denotes the rotation speed calculated based on the computed airflow velocity, which is 21.22 rps.

3.2 Numerical Method

In this study, numerical simulation was carried out using XFlow software based on large eddy simulation (LES) and particle dynamic solvers for solving the equation of Boltzmann transport as follows (Chávez-Modena et al., 2020):

$$\frac{\partial f_i}{\partial t} + e_i \cdot \nabla f_i = \Omega_i, i = 1, \ldots, b \tag{1}$$

To the direction i, f_i is the particle distribution function, e_i denotes the discrete velocity that corresponds, and in the formula, Ω_i is the collision operator.

In LES calculations, the sub-grid eddy-viscosity model used the wall-adapting local eddy-viscosity (WALE) model to accurately simulate near-wall and far-wall regions as well as laminar and turbulent characteristics. Furthermore, a turbulent eddy viscosity v_t was used in turbulence modeling and founded on the LBM solver. This viscosity is expressed as follows (Ren et al., 2013):

$$v_t = \Delta_f^2 \frac{\left(G_{\alpha\beta}^d G_{\alpha\beta}^d\right)^{3/2}}{\left(S_{\alpha\beta} S_{\alpha\beta}\right)^{5/2} + \left(G_{\alpha\beta}^d G_{\alpha\beta}^d\right)^{5/4}} \tag{2}$$

Where the constant c_ω typically equals 0.325, the filter scale is $\Delta f = c_\omega \Delta x$, the strain rate tensor of the resolved scales $S_{\alpha\beta} = \frac{1}{2}\left(\frac{\partial v_\alpha}{\partial r_\beta} + \frac{\partial v_\beta}{\partial r_\alpha}\right)$ and the $G_{\alpha\beta}^d = \frac{1}{2}\left(g_{\alpha\beta}^2 + g_{\beta\alpha}^2\right) - \frac{1}{3}\delta_{\alpha\beta} g_{\gamma\gamma}^2$.

The non-equilibrium enhanced wall function was used to estimate flow velocities in the vicinity of the wall, thereby decreasing the computational requirements for determining the near-wall flow field parameters.

The model length and speed ($U_0 = 10$ m/s) indicated that the Reynolds number was approximately 3.58×10^5. The overall simulation time was $T = 1$ s, and the time step was calculated automatically to be $\Delta t = 7.69231 \times 10^{-5}$ s; thus, numerical stability was guaranteed.

3.3 Data Processing

The force coefficients were dimensionless for comparative investigation in the following ways:

$$C_D = \frac{F_D}{\frac{1}{2}\rho U_f^2 S} \tag{3}$$

$$C_P = \frac{P - P_0}{\frac{1}{2}\rho U_f^2} \tag{4}$$

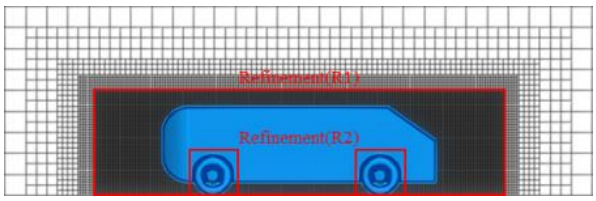

(a) Sideview

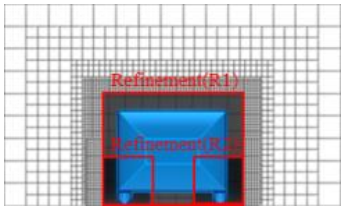

(b) Front view

Fig. 7 Refinement boxes around the car model

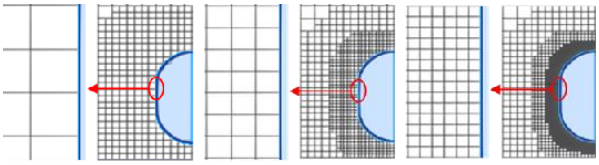

(a)Coarse (b)Medium (c) Fine

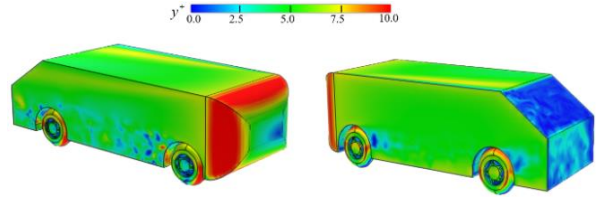

(d) Values of y+ around the model surface

Fig. 8 Different grid resolutions around the model

$$U = \frac{\sqrt{\left(U_f - U_x\right)^2 + U_z^2}}{U_f} \tag{5}$$

$$u_l = \frac{U_{local}}{U_f} \tag{6}$$

Where C_D denotes the drag coefficient averaged over time, C_P is the coefficient of pressure, U represents the coefficient of slipstream speed, and u_l means the spatial velocity coefficient. Moreover, F_D is the aerodynamic drag; P is the time-averaged hydrostatic pressure on the surface of the car model, and P_0 represents the reference pressure. Finally, U_f is the inlet wind speed, and U_x and U_z are the wind speeds in the X-direction and Z-direction, respectively; U_{local} denotes the wind speed around the model; and ρ represents the air density.

3.4 Grid Strategy

The adaptive lattice structure of XFlow dynamically adjusted its lattice resolution to the flow pattern when the wheel rotation drastically changed the surrounding flow field. As shown in Fig. 7, three refinement boxes (R, R1, and R2) are used to guarantee accurate capture of the detailed flow features. The size of the R1 was 1.044 m × 0.261 m × 0.261 m, while that of the R2 was 0.095 m × 0.085 m × 0.085 m. Wheel rotation causes a gradual change in the wake region's pressure gradient and velocity. Consequently, the detailed variation of the wake flow was captured employing the lattice adaptive refinement function of XFlow. The details of the three resolution strategies are shown in Fig. 8. The initial grid numbers of coarse, medium, and refined were 1.15, 2.64, and 6.13 million cells, respectively, and the details of different grid resolutions are shown in Table 1. In the distant field, the resolution h was fixed at 0.04 m. The accuracy of the numerical method was further verified, and the boundary layer flow was accurately predicted by setting the minimum mesh size closest to the surface of the model, which resulted in y^+ being approximately 10 for the majority of the surfaces, as depicted in Fig. 8(d).

Table 1 Details of different grid resolutions

Grids	R	R1	R2	Grid number (×10^6)
Coarse	h/2^2	h/2^3	h/2^4	1.15
Medium	h/2^3	h/2^4	h/2^5	2.64
Fine	h/2^4	h/2^5	h/2^6	6.13

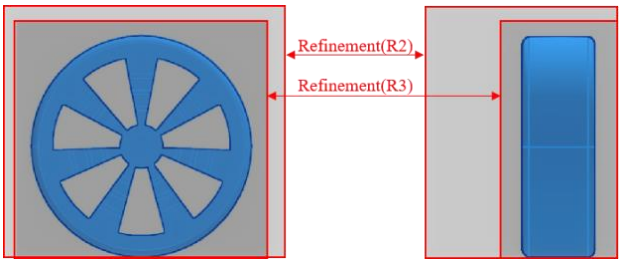

(a) The location and size of the refinement region

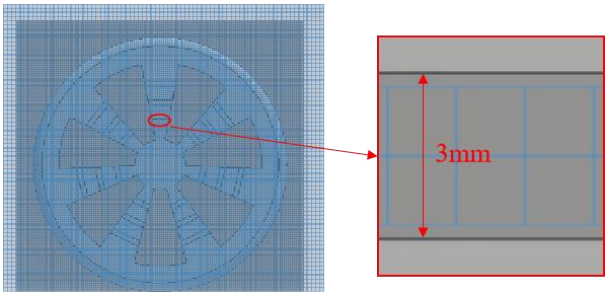

(b)The medium grid resolutions on the grooves

Fig. 9 Refinement grid regions around the wheel

To accurately obtain the flow characteristics around the designed groove structure in section 3.6, a new refinement region, namely R3, was added around the wheel. As displayed in Fig. 9(a), the size of R3 was 0.065 m × 0.08 m × 0.08 m, and Fig. 9(b) details the groove's medium grid resolutions. The dimensions of the model used for the wind tunnel test were enlarged to a ratio of 2:1, and the length, width, and height of the Ahmad model were adjusted to 1.044 m, 0.389 m, and 0.288 m in that order. This study explored the effects of the spoke

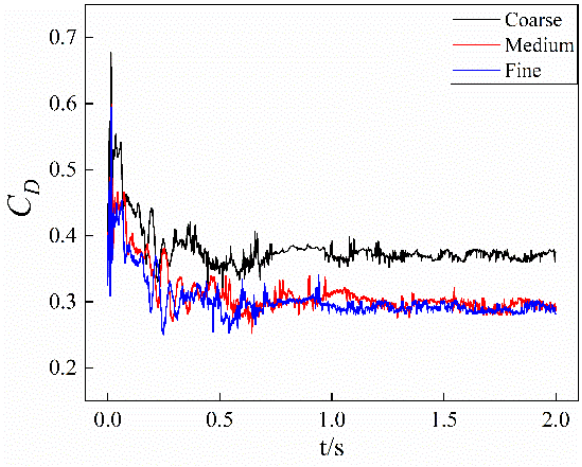

(a) Time history curves of drag coefficient calculation

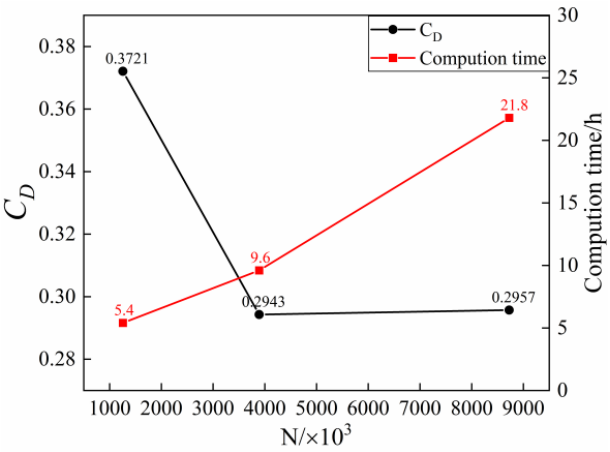

(b) The influence of particle number on drag coefficient and calculation time

Fig. 10 Simulation results of different grid schemes

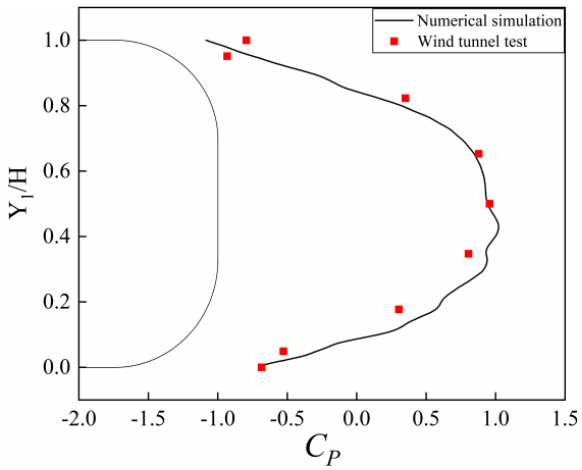

(a) The front

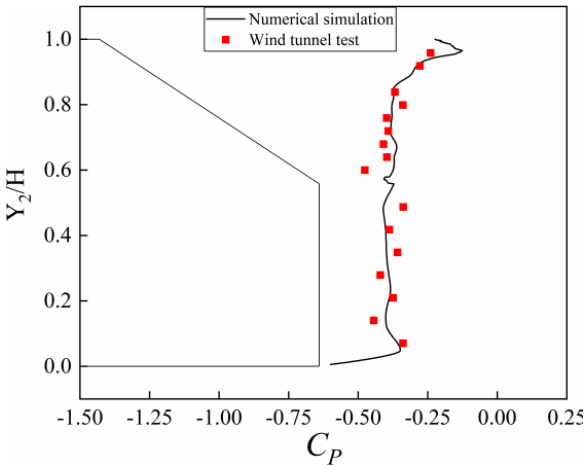

(b) The tail

Fig. 11 Comparisons of the pressure coefficient distributions between the wind tunnel test and numerical simulation

structure on the aerodynamic characteristics of the aforementioned model under high wind speeds. The inflow velocity is 40 m/s, and the Reynolds number is approximately 2.78×10^6, which is consistent with the work of Huminic and Huminic (2017). Based on the speed of the air velocity and the size of the wheels, the wheel rotational velocity was determined to be 84.88 rps.

3.5 Mesh Sensitivity and Numerical Validation

The medium and fine mesh simulation results are closer in Fig. 10(a), where the drag coefficient gradually converges with increased simulation time. The 1-2 s drag coefficient was calculated as the mean value. According to Fig. 10(b), the drag coefficient progressively started to stabilize as the number of particles and computation time increased significantly with continuous grid refinement. The medium mesh scheme was chosen as the numerical simulation method in this research based on accuracy and computational resources, and further experimental verification was carried out.

Figure 11 compares the pressure coefficients calculated for the longitudinal central section of the simulated model by using the medium-resolution grid scheme. The vertical coordinates are expressed as the ratio of the heights of the measurement points (Y_1, Y_2) to the height of the vehicle body (H), and the horizontal coordinates are expressed as the pressure coefficients of the measurement points. The model's simulated front-end pressure coefficients better matched the test data, as can be seen in Fig. 11. The influence of the wind tunnel test bench may lead to minor deviations in the individual calculations. At the tail end of the model, slight discrepancy was noted between the simulation and experimental results. This discrepancy occurred because not all numerical and experimental settings were the same; differences between wind tunnel and computational domain caused variations in ground boundary layer thickness development. However, the simulated pressure coefficient distribution trend is generally consistent with the wind tunnel tests; the root-mean-square errors for the front and tail of the model were 16.32% and 4.53%, respectively, and the overall variation trend has been well predicted. Therefore, it can be concluded that the medium mesh numerical strategy proposed in this paper was sufficient for obtaining accurate simulation results.

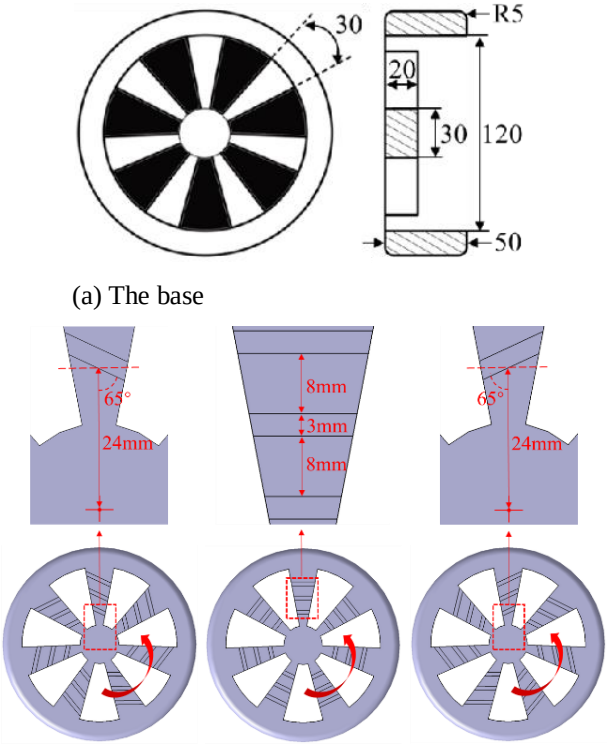

(a) The base

(b) The Case1 (c) The Case2 (d) The Case3

Fig. 12 Base model and non-smooth grooves designed model for wheel spokes

3.6 Design and Modeling of Groove Spoke

In order to make this study more closely fit the actual wheel shapes, and based on the results of wheel configuration affect aerodynamic drag (Zhou et al., 2024), a wheel with an opening area of 50% was selected as the research object, and Fig. 12(a) shows the main sizes of the wheel; the outer diameter of the wheel is 150 mm, and the width of the wheel is 50 mm. Additionally, the spoke thickness is 20 mm, the spoke diameter ranges from 30 to 120 mm, and the angle between neighboring spokes is established as 30°. Based on the wheel with a smooth surface in Fig. 12(a), three forms of groove structures with different directions are carved on the spoke surface. As shown in Fig. 12(c), wheels designed with horizontal grooves, named Case 2, the width of the groove is 3 mm, and the distance between adjacent grooves is 8 mm. Based on the theory of reducing the resistance of the boundary layer in fluid engineering fluid mechanics, the depth of the groove is set at 2 mm. The three grooves are arranged horizontally and equidistant from the centre of the wheel in turn outwards. Under the condition of keeping the spacing constant, the horizontal grooves are rotated respectively by 25° clockwise and anticlockwise to form the forward groove and reverse groove shapes, as shown in Fig. 12(b) and (d), and named them Case1 and Case3, respectively.

4. NUMERICAL RESULTS

4.1 Aerodynamic Drag

The influence of different groove designs upon the

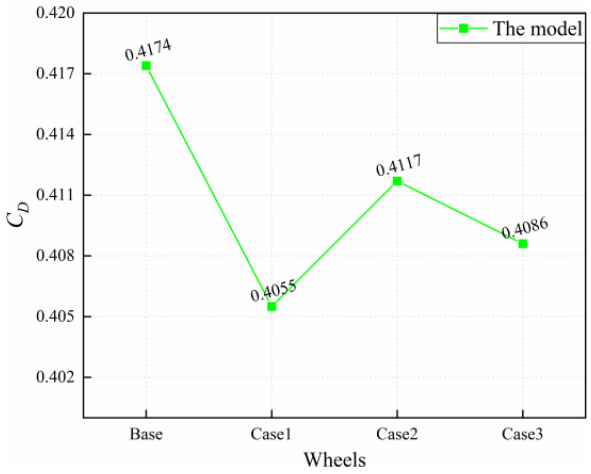

(a) The car model

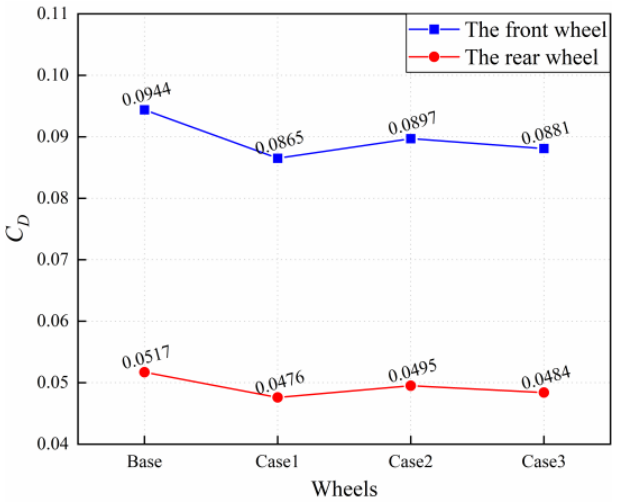

(b) The front and rear wheels

Fig. 13 Comparison of drag coefficients

wheels and the vehicle model's coefficients of drag is shown in Fig. 13. In Fig. 13(a), as for the original (the Base) car model, the C_D value was 0.4174. The C_D values of the car model for Case1, Case2, and Case3 were 0.4055, 0.4117, and 0.4086, respectively. The groove structure in Case 1 exhibited the most significant drag reduction effect with 2.85%. Nevertheless, Case 2 and Case 3 had comparatively lesser effects on drag reduction, and the C_D values of the car models reduced by 1.37% and 2.21%, respectively. As seen from Fig. 13(b), the groove structures could also reduce the aerodynamic drag of the front and rear wheels, and the front wheels had a higher drag coefficient than the rear wheels. This result indicates that the air resistance of an automobile is more strongly affected by its front-wheel configuration than by its rear-wheel configuration. The Base had a C_D of 0.0944 for the two front wheels and a C_D of 0.0517 for the two rear wheels. The drag coefficients for the front and rear wheels of Case 1 were 0.0865 and 0.0476, and the C_D was reduced by 8.37% and 7.93%, respectively, with the largest reduction in the three grooves.

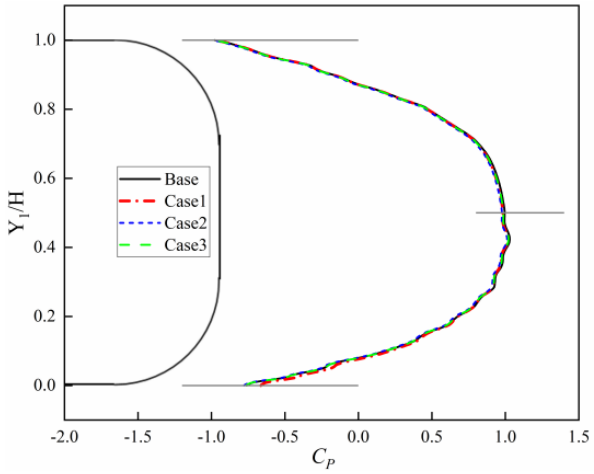

(a) Model front-end

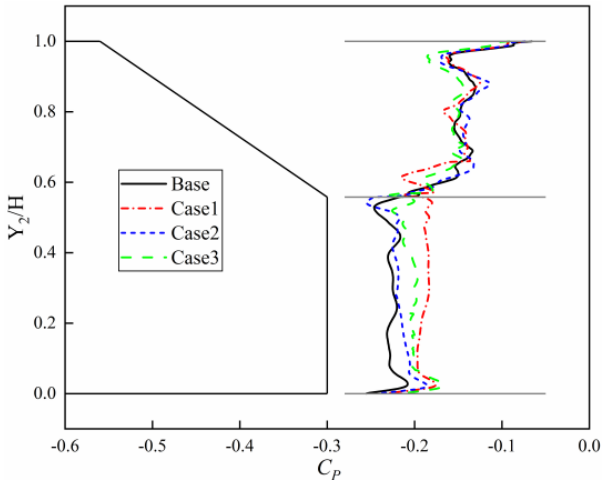

(b) Model tail

Fig. 14 Comparison of model centerline mean pressure coefficient

4.2 Flow Fields Around the Car Model

Figure 14 depicts the time-averaged pressure distributions along the centerlines of the front and rear ends of the car model. Positive pressures were observed at the front end because of the airflow at the blunt head within the front end. Subsequently, the airflow moved back along the blunt head, initiating flow separation and causing a gradual decrease in surface pressure. It was evident that the base and three cases had nearly identical pressure on the surface distributions in the front-end areas of the car bodywork. The flow grew more complicated and disordered after the airflow traveled to the rear areas, and the flow separation became severe. Afterward, the car model's vertical plane and slant plane displayed negative pressure. Notably, as Fig. 14(b) demonstrates, the vertical plane's pressure distribution was lower than the slant plane's. Furthermore, the pressure coefficient at the rear of the car model corresponding to the three cases was higher than that of the base, especially the vertical plane. By contrast, the pressure coefficient on the slant plane did not change significantly. Meanwhile, the pressure coefficient on the vertical plane of Case1 increased most obviously.

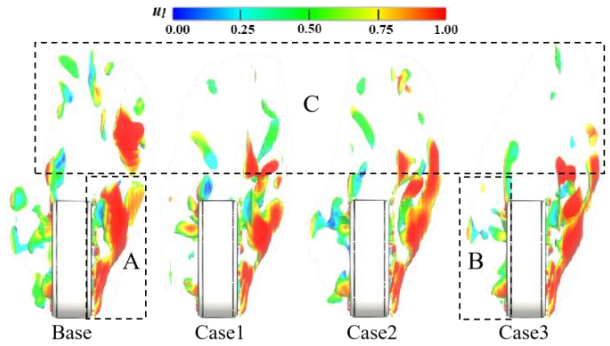

(a) The front wheel

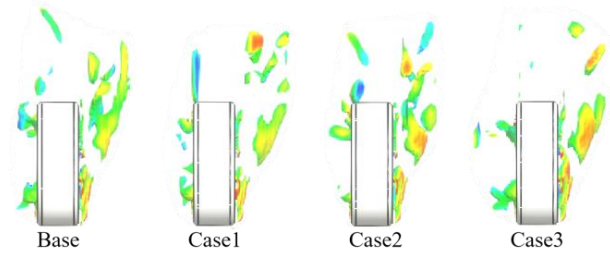

(b) The rear wheel

Fig. 15 Iso-surfaces of a vortex around the wheel (Q = 60000)

The results of the vortex development around the front and rear wheels under various groove structures are presented in Fig. 15. The second invariant—namely the Q criterion—was applied to the iso-surface of vortex shells. With the time-averaged flow velocity U_l, the iso-surface of Q is presented in Fig. 15. Equation (7) defines the Q criteria:

$$Q = -\frac{1}{2}\left(S_{ij}S_{ij} - \Omega_{ij}\Omega_{ij}\right) \tag{7}$$

Where S_{ij} and Ω_{ij} are the symmetric and anti-symmetric parts of the velocity gradient tensor, respectively.

Figure 15 indicates the influence of the designed grooves on the vortex distribution around the front and rear wheels. In Fig. 15(a), these grooves strongly influenced the flow features and vortex formation around the wheels. On the outer side of the wheel, the groove structures reduced the generation of large vortices and promoted the separation of the original large vortices into more small vortices, as shown in the wheel's outer side region A. In region B of the wheel's inner side, the grooves weakened the vortices and enhanced their dispersion. Moreover, it was also worth noting that there was a difference in the wake in region C. The grooves reduced the breakup and shedding of the wake vortex, thereby decreasing the extensiveness of this vortex. The wake vortex produced in Cases 1–3 resulted in less flow fluctuation than that produced in the base case. All grooves used in this study improved the vortex distributions. Among these grooves, those used in Case 1 produced the best vortex distributions in all model regions, especially Regions B and C; these grooves delayed flow separation and weakened energy dissipation. Among the four cases, the car model and wheels had the lowest

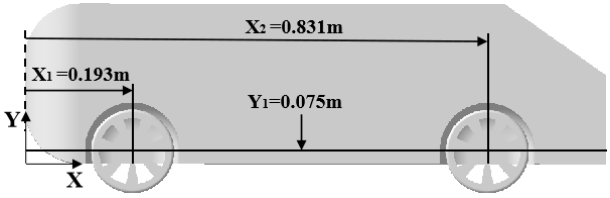

Fig. 16 Locations of the cross-sections and horizontal plane

aerodynamic drag in Case 1, as shown in Fig. 13. In this case, the airflow around the front wheels created vortices that traveled backward along the flow direction. Figure 15(b) illustrates the reduced airflow velocity and weakened vortices around the rear wheels. In this case, fewer large vortices and more dispersed vortices were produced at the rear wheels than at the front wheels. Thus, the aerodynamic drag of the rear wheels had a relatively small effect on the aerodynamic performance of the car. Overall, the grooves improved the vortex distributions around the rear and front wheels, especially on the inner side of these wheels.

The two components that make up aerodynamic drag for the car model are pressure drag and viscous drag, which have a direct relationship with boundary-layer thickness, and are one of the sources of aerodynamic drag, thus, Fig. 16 displays the specific positions of the two cross-sections and one horizontal plane chosen to investigate boundary layer thickness and flow distribution surrounding wheels and the car model.

The 0.99*U* boundary layer thickness at the horizontal plane of Y_1 = 0.075 m across the front and rear axle centers are depicted in Fig. 17(a), and it was clear from this figure that the thickness of the boundary layer grew progressively throughout the overall length of the model. Moreover, it could be seen that the boundary layer thicknesses in the three cases were less than those of the base, with the thickness being lowest in Case 1 and then in Case 3. The boundary layer thickness also gradually increased from the front wheels to the rear wheels, as shown in Fig. 17(b)and(c). It should be noted that the boundary layer thickness of Case 1 was still the smallest among the three cases and the base, similar to Fig. 17(a).

The longitudinal plane of the model (Y_1 = 0.075 m) and the cross-sectional of the model (X_1 = 0.193 m and X_2 = 0.831 m) in Fig. 18 display the time-averaged flow lines for investigating the impact of different groove structures on the flow distribution. Figure 18(a) indicates that the primary components of the vortex structure were two recirculation regions, V_1 and V_2 in the wake and V_3 close to the vertical plane. Moreover, a minor vortex was present near the slant plane. The airflow at the top of the model flows downward along the slant pane. Because of the low pressure in the wake, a portion of the airflow formed vortex V_1, while most of the airflow was entrained by the vertical rear low pressure, combined with airflow entering the bottom to form vortices V_2 and V_3. The impact radius of V_1 and V_2 were smaller in Cases 1–3 than in the base case. Among all vortices, V_3 exhibited the largest change, and V_3 was smaller in Cases 2 and 3 than in the base case.

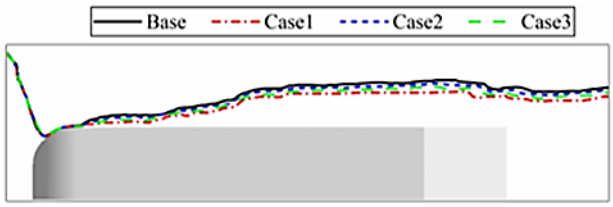

(a) horizontal plane at Y_1=0.075m

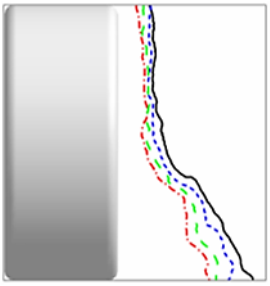

(b) cross sections at X_1=0.193m

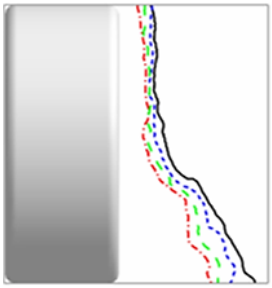

(c) cross sections at X_2=0.831m

Fig. 17 Boundary layer thickness around the car model

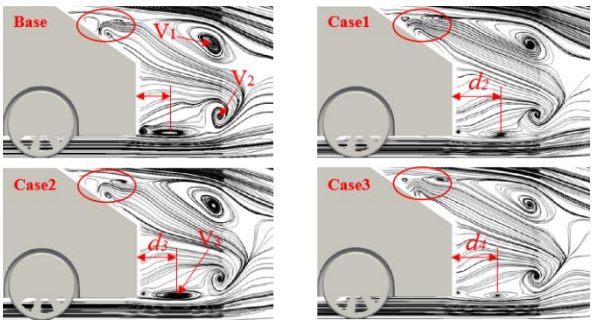

(a) Streamlines in the longitudinal plane at Z=0 m

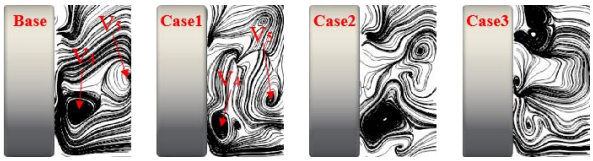

b) Streamlines in the cross sections at X_1=0.193 m

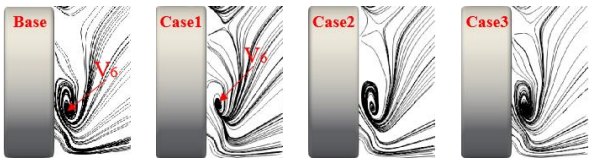

(c) Streamlines in the cross sections at X_2=0.831m

Fig. 18 Comparison of time-averaged streamlines distributions

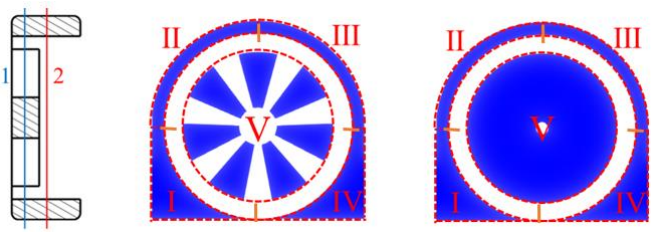

Fig. 19 Cross-section location and region division of the wheel

Moreover, the distance between the center of the vortex V3 and the vertical plane was also increased, and the order of the distance was as follows: $d_2>d_4>d_3>d_1$. The position of the vortex center at the rear end moved backwards, which improved the flow structure of the wake and increased the surface pressure on the vertical plane. Thus, the model was subject to less aerodynamic drag, which agrees with the results displayed in Fig. 14. The front and rear wheel regions depict the distributions of streamlines in Fig. 18(b) and (c), respectively, and the flow around the wheel was more complicated. The wheel hindered the airflow, and flow separation occurred in the near-ground area. The jet vortices were generated, as shown in V_4 and V_5, especially at the base wheel. The grooves on the surface of the wheels changed the vortex structure and promoted the dispersion of large and small vortices. For example, vortex V_4 had a better structure in Case 1 than in the base case. The rear wheels had a superior streamline distribution relative to the front wheels because of the reduced airflow, and vortex V_6, which was similar to vortex V_4, was still in the near-ground area. The streamline distribution at the rear wheels in Cases 1–3 was better than that in the base case, with the best results being obtained in Case 1, as shown in Fig. 18(c).

4.3 Study and Evaluation of Flow Stability

4.3.1 Energy Gradient Theory

Energy gradient theory, which was formulated by Dou Hua-Shu, describes changes caused in the magnitude and direction of mechanical energy gradients by flow stability and turbulent transitions within the flow field (Dou & Phan-Thien 2007; Dou et al., 2008; Dou & Jiang 2013). At present, energy gradient theory is primarily used to analyze flow instability processes and the influence of design parameters on flow stability in centrifugal pumps (Chen et al., 2019; Li et al., 2019). The energy gradient theory was implemented to analyze and evaluate the flow stability in the wheel region, taking into account that the motion characteristics of the rotating wheel and the blades inside a centrifugal pump are similar.

Let n represent the normal direction of the streamlines, and s represent the tangential direction. The energy gradient parameter K can be expressed as follows (Xiao et al., 2016):

$$K=\frac{\frac{\partial P}{\partial n}+\rho U\frac{\partial U}{\partial n}}{\frac{\mu_t}{U}\left(\frac{\partial U}{\partial n}\right)^2-\frac{2\mu_t}{\rho U^2}\frac{\partial U}{\partial n}\frac{\partial P}{\partial n}+\frac{\mu_t}{\rho^2U^3}\left(\frac{\partial P}{\partial n}\right)^2} \tag{8}$$

The equation $\partial E/\partial n$ represents the energy gained by a unit fluid element along the direction normal to the streamlines, $\partial H/\partial s$ denotes the energy lost by a unit fluid element along the direction tangential to the streamlines, P is the static pressure measured in Pa scales, and ρ is the fluid density. $U=\sqrt{u^2+v^2+w^2}$, where u represents the velocity of the fluid along the X-axis, v represents the velocity of the fluid along the Y-axis, and w represents the velocity of the fluid along the Z-axis, measured in units of m/s. μ_t represents the turbulent viscosity, measured in units of Pa·s. At standard atmospheric pressure and a temperature of 20°C, the viscosity of air is approximately 1.79×10^{-5} kg/(m·s), and the viscosity of water is approximately 1.01×10^{-3} kg/(m·s).

4.3.2 Energy Gradient Function *K* Value

Two cross sections in the wheel regions, namely Cross Sections 1 and 2, were selected to evaluate the energy gradient function (K). As displayed in Fig. 19, Cross Section 1 was located at half the thickness of a spoke, whereas Cross Section 2 was located at half the thickness of a wheel. The influence of the opening area of the spokes was also considered. Each wheel was divided into five zones, with Region V representing the spoke structure.

Figure 20 and Figure 21 display the distributions of K values in Cross Sections 1 and 2 of the front and rear wheels, respectively. The red area is the area with the larger value of the K function. A larger value of K corresponds to higher turbulence intensity and poorer flow stability (Dou 2016). Figure 20 proves that the regions with larger K values were mainly distributed in the inner Region III of the wheel cavity on the upper right and the spoke structure Region V, indicating that the airflow through the wheel began to lose stability at these two places first. Compared with the base wheel, three types of groove structures effectively reduced the areas with large K values. They enhanced the flow stability near the front wheel, among which Region III and Region V of Case1 were the most significant from an energy perspective. The groove structures not only reduced the K values around certain regions of the front wheels (such as in regions III and V of Cross Section 1) but also transformed larger areas of flow instability around these wheels into smaller dispersed areas of instability (such as Region V of Cross Section 2). Thus, these structures improved the flow stability around the front wheels, reduced energy dissipation losses, and decreased the overall aerodynamic drag of the vehicle.

In contrast, the overall flow characteristics of the rear wheels in Fig. 21 were relatively stable. No obvious

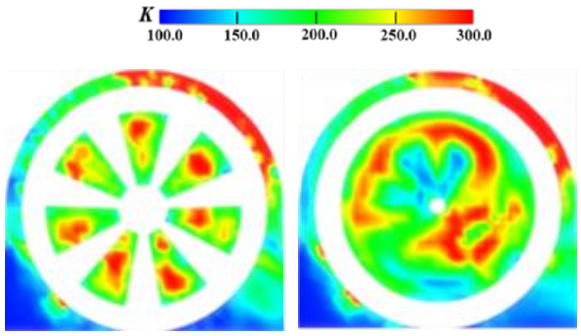

(a) Base

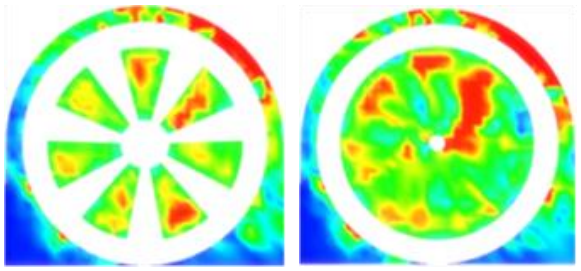

(b) Case 1

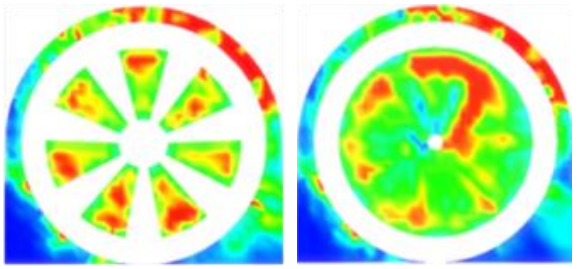

(c) Case 2

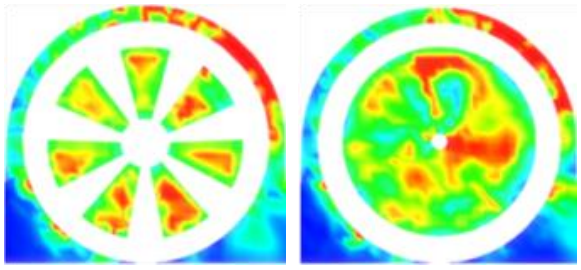

(d) Case 3

Fig. 20 The *K* value distribution of the front wheel sections (Left: Section 1; Right: Section 2)

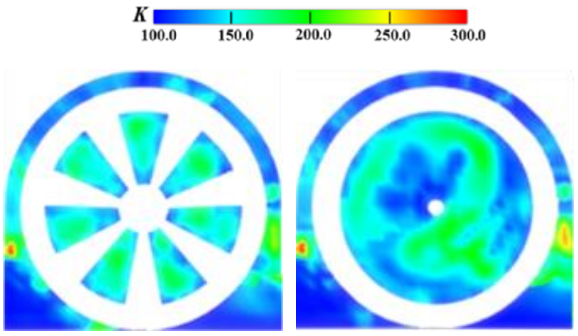

(a) Base

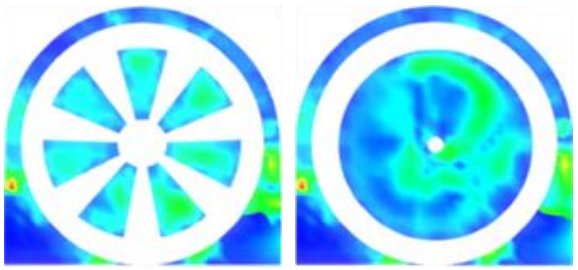

(b) Case 1

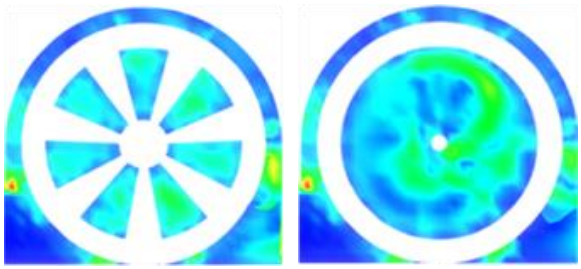

(c) Case 2

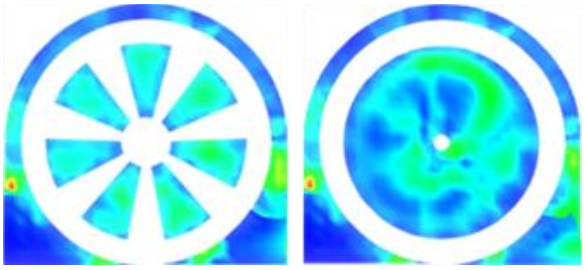

(d) Case 3

Fig. 21 The *K* value distribution of the rear wheel sections (Left: Section 1; Right: Section 2)

variation in the *K* value distribution near the wheel cavity entrances and exits was observed, whereas the three groove structures added to the spokes decreased the larger *K* value distribution area in Region V and strengthened the flow stability in this region, thereby lowering the aerodynamic drag of the wheel, which was similar to that of the front wheels.

5. DISCUSSION OF RESULTS

5.1 Aerodynamic Drag and Flow Fields

In Fig. 13, the C_D values of the front and rear wheels kept the same change trend as that of the car model, indicating that the aerodynamic performance of the wheels influenced the aerodynamic characteristics of the car. Thus, aerodynamic optimization of the wheels can improve the aerodynamic performance of the vehicle. It can be inferred that in a given groove size and structure, the groove arranged at a reasonable direction angle could obtain a greater effect of drag reduction to improve the aerodynamic performance of the car model and wheel. The results also suggested that the aerodynamic drag of this car model was caused by the pressure drag acting on its front and rear ends. A comprehensive comparison of the findings in Fig. 14(a) and (b) indicated that the higher the pressure coefficient at the rear of the model, the smaller the aerodynamic drag, in which Case1 was the

least, which corresponded with Fig. 13, drag coefficients of the fluctuating tendency of the car model. The pressure distribution difference proved that flow field properties variations caused drag coefficient variations.

The difference in boundary layer thickness combining Fig. 16 and Fig. 17 indicates that wheel-carved grooves affect not only the flow fields surrounding the wheel but also the flow features surrounding the car model. Furthermore, the boundary layer thickness reduced with decreasing distance to the rear of the model and grew with decreasing distance to the ground; the aerodynamic drag decreased. Thicker boundary layers positively correlate with aerodynamic drag; the thicker the boundary layer, the higher the drag. The contour characteristic of the boundary layer elucidated the reason behind the lowest aerodynamic drag in Case 1. among the three cases and the base model. In general, the groove structure influenced the flow state near the wall. It led to decreased aerodynamic drag, probably because the groove structure reduced the intensity and instability of the turbulent boundary layer, thereby hindering the development of the turbulent boundary layer.

5.2 Relationship Between Flow Stability and Aerodynamic Drag

Airflow separation occurred in the unstable-flow regions displayed in Figs. 20 and 21. As air flowed through adjacent spoke gaps and wheel cavities, frequent flow separation and reattachment occurred because of wheel rotation and velocity gradients. This unstable flow resulted in the formation of vortex structures that increased the drag from air circulation. These localized vortex structures created high and low-pressure zones; the pressure difference caused a more significant drag effect. Moreover, promptly dissipating the vortices surrounding the wheel cavities was difficult. Therefore, a continuous drag effect was produced that increased the aerodynamic drag. Furthermore, the unstable-flow regions enhanced the turbulence effect. When the airflow passed through the gap between the wheel cavity and the wheel housing gap, the airflow was disturbed by the wheel rotation and the geometrical irregularity of the wheel housing gap, which restricted the smooth passage of the airflow, making the flow extremely unstable. The degree of flow turbulence increased in the region, thus enhancing the turbulence intensity. The airflow's momentum dissipation was increased, leading to larger differential pressure resistance and viscous drag. As the airflow ran through the wheel cavities and wheel housing gap, velocity fluctuations occurred in different regions, triggering an unsteady velocity gradient. This gradient caused an increase in the shear stress, which increased the aerodynamic drag.

To examine the effect of the wheel spoke structure on the flow stability in different wheel regions, the average *K* values of the five same regions were calculated and compared. Figure 22 compares the average *K* values of the same regions in the groove structure wheel for the two cross-sections. All three spoke groove designs significantly reduced *K* values in Region III and Region V of the wheel. The forward groove wheel showed the most significant reduction in *K* values, followed by the reverse groove, while the transverse groove had the smallest

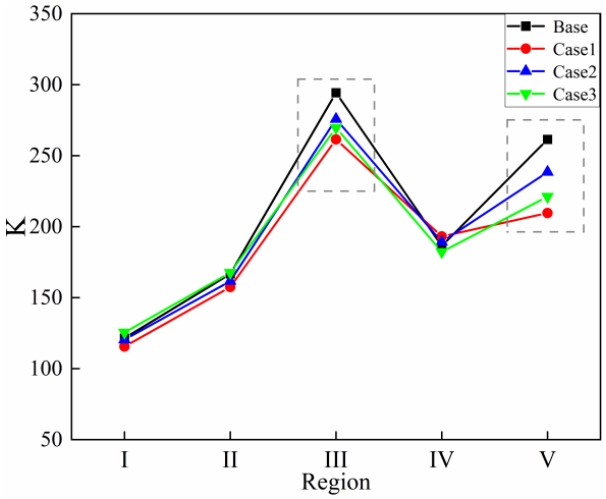

(a) The front wheel

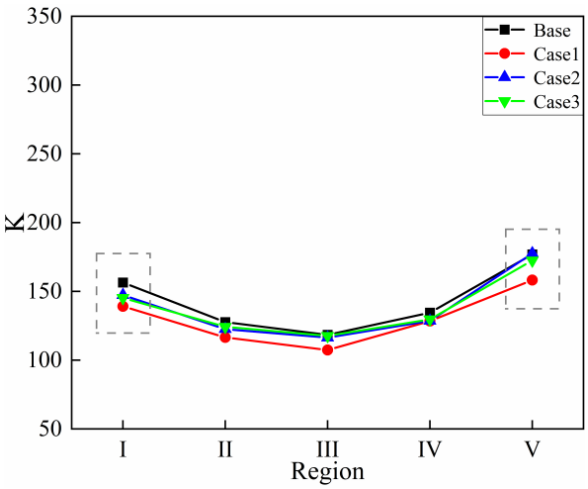

(b) The Rear wheel

Fig. 22 Comparison of average K values in different regions

reduction. The grooves did not cause notable changes in the *K* values of the other three regions. In contrast, in Fig. 22(b), the forward groove wheel exhibited the lowest K values in all five regions, with the largest reduction observed in Region V, while the *K* values in the five regions of the other two groove wheels showed relatively smaller changes.

Section 4.3 examined and analyzed the influence of non-smooth grooves on the overall drag coefficient of the considered car model and on the flow stability in the wheel regions of this model. The wheel region's flow stability was evaluated using the energy gradient function. The results indicated that certain regions of the wheel experienced significant flow instability, greatly influenced by the non-smooth surface structures. Therefore, to understand the relationship between the flow stability in the wheel regions and the overall aerodynamic drag of the car from an energy perspective, the *K* values in the wheel regions with severe flow instability and the overall drag coefficient of the car were analyzed concurrently.

Figure 23 illustrates the influence of the designed groove structures on the overall drag coefficient of the car

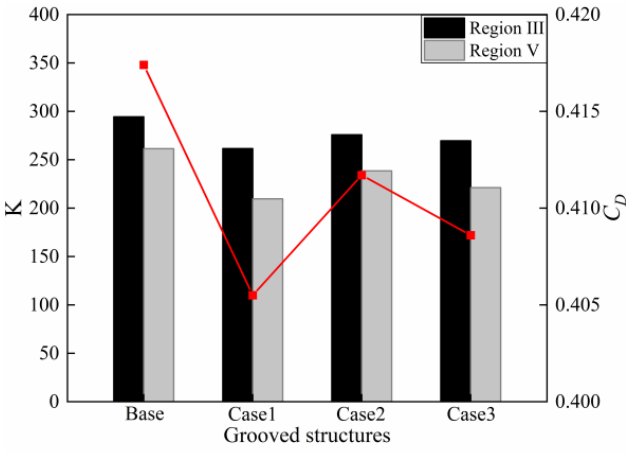

(a) The front wheel

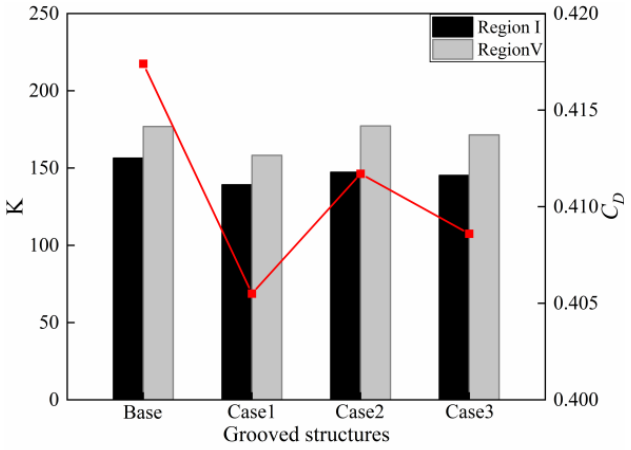

(b) The rear wheel

Fig. 23 Comparison of the K value and drag coefficient under different spoke groove structures

and the *K* values in specific wheel regions with severe flow instability. It should be noted that this study only considers two regions in the front and rear wheel areas where flow instability is more severe. The *K* values of region III and region V for the front wheel and region I and region V for the rear wheel were compared with the overall drag coefficient of the vehicle. From Fig. 23, the overall drag coefficient of the car was positively correlated with the flow stability in the front and rear wheel regions. As *K* increased (decreased), flow instability became more (less) severe, and the overall drag coefficient of the car increased (decreased).

6. CONCLUSION

In this study, numerical analysis and wind tunnel testing were conducted to examine the pressure distribution on a car model using the Ahmed model. The numerical results were in agreement with the experimental results, which confirmed the accuracy of the numerical method. Subsequently, wheel spokes with three types of bionic non-smooth grooves were designed, and the effects of these grooves on the fluid dynamics and aerodynamic drag of the wheel and car model were numerically investigated. Furthermore, energy gradient theory was used to assess the flow stability in different wheel regions, and the relationship between the energy gradient function (*K*) and the aerodynamic drag of the car was determined.

The three types of designed grooves reduced the aerodynamic drag of the wheels and car. Among these grooves, forward grooves (Case 1) exhibited the strongest drag reduction effect, reducing the drag coefficients of the front wheels, rear wheels, and overall car by 8.37%, 7.93%, and 2.85%, respectively. Moreover, an investigation of the boundary layer thicknesses around the wheel and the car model indicated that after attaching the groove structure to the wheel spokes, the three types of designed grooves reduced these thicknesses, with the smallest thicknesses again observed in Case 1.

The analysis of the vortex structure around the wheels using the *Q* criterion revealed that the groove structure diminished the generation of large vortices on the wheel's outer side, weakening the intensity of vortices on the inner side and the fluctuation of the wake, thus decreasing the energy consumption in turn to reduce the drag, the Case 1 having the most obvious improvement effect. The energy gradient theory was employed to analyze the *K* values distribution in the wheel region. Compared to the base wheel, the groove structure reduced *K* values, thereby improving flow stability around the wheel. The *K* values of five different regions in the wheel were also analyzed, and the flow fluctuations in the front wheel were greater than those of the rear wheel. Moreover, the *K* values in front- and rear-wheel regions with severe flow instability had a positive correlation with the overall vehicle drag coefficient.

The key findings of this study are: using the bionic drag reduction mechanism as a reference, the groove structures with appropriate number, inclination angle, and depth were designed on the wheel spoke surfaces, which realized the flow stability improvement and aerodynamic drag decrease effectively of the wheel region. Moreover, the positive correlation between the flow stability of the wheel region and the aerodynamic drag coefficient of the entire vehicle was revealed by using the energy gradient function *K* value. This research implies that the bionic non-smooth structural design of wheel spokes has enhanced the aerodynamic efficiency and fuel economy of the vehicle, which provided theoretical references with practical value for the wheel structural design in real-world passenger vehicles and boosted the conceptual development of energy-saving and environmental protection of the automobile.

Some limitations will be considered in future work. For example, the other bionic non-smooth surface structures and the response parameters optimization of the non-smooth surface structure will be carried out to achieve the maximum drag reduction, and the aerodynamic noise performance of the car with the bionic wheel should also be explored.

ACKNOWLEDGEMENTS

The authors acknowledge the computing resources provided by the China Automotive Engineering Research Institute Co. Ltd, Chongqing.

CONFLICT OF INTEREST

No potential conflict of interest was reported by the author (s).

AUTHORS CONTRIBUTION

Tinghui Huang: Conceptualization, Software, Methodology, Formal analysis & Discussion, Writing - original draft preparation, Validation, Writing - review & editing. **Haichao Zhou**: Conceptualization, Methodology, Formal analysis & Discussion, Validation, Writing - review & editing. **Jian Yang:** Discussion, Supervision. **Wei Zhang:** Visualization and Discussion. **Qingyun Chen:** Supervision.

FUNDING

All the authors were pleased to acknowledge funding from the National Natural Science Foundation of China (No. 52072156, No. 52272366). And the Postdoctoral Foundation of China (2020M682269).

REFERENCES

Ahmed, S. R., Ramm, G., & Faltin, G. (1984). Some salient features of the time-averaged ground vehicle wake. *SAE Transactions*, 473-503. https://www.jstor.org/stable/44434262

Beaudoin, J. F., & Aider, J. L. (2008). Drag and lift reduction of a 3D bluff body using flaps. *Experiments in fluids*, *44*(4), 491-501. https://doi.org/10.1007/s00348-007-0392-1

Blacha, T., & Islam, M. (2017). The aerodynamic development of the new Audi Q5. *SAE International Journal of Passenger Cars-Mechanical Systems*, *10*(2017-01-1522), 638-648. https://doi.org/10.4271/2017-01-1522

Bolzon, M. D. P., Sebben, S., & Broniewicz, A. (2019). Effects of wheel configuration on the flow field and the drag coefficient of a passenger vehicle. *International Journal of Automotive Technology*, *20*(4), 763-777. https://doi.org/10.1007/s12239-019-0072-1

Brandt, A., Berg, H., Bolzon, M., & Josefsson, L. (2019). The effects of wheel design on the aerodynamic drag of passenger vehicles. *SAE International Journal of Advances and Current Practices in Mobility*, *1*(2019-01-0662), 1279-1299. https://doi.org/10.4271/2019-01-0662

Chávez-Modena, M., Martínez, J. L., Cabello, J. A., & Ferrer, E. (2020). Simulations of aerodynamic separated flows using the lattice Boltzmann solver XFlow. *Energies*, *13*(19), 5146. https://www.mdpi.com/1996-1073/13/19/5146

Chen, X., Zhu, Z., Dou, H. S., & Li, Y. (2019). Large eddy simulation of energy gradient field in a centrifugal pump impeller. *Proceedings of the Institution of Mechanical Engineers, Part C: Journal of Mechanical Engineering Science*, *233*(11), 4047-4057. https://doi.org/10.1177/0954406218809127

Chok, C., Parameswaran, S., Sun, R., & Gleason, M. (1994). Numerical investigation of the effects of base slant on the wake pattern and drag of three-dimensional bluff bodies with a rear blunt end. *Journal of wind engineering and industrial aerodynamics*, *51*(3), 269-285. https://doi.org/10.1016/0167-6105(94)90063-9

Dou, H. S. (2016). A universal equation for calculating the energy gradient function in the energy gradient theory. *arXiv Preprint arXiv*:1610.01517. https://doi.org/10.48550/arXiv.1610.01517

Dou, H. S., & Jiang, W. (2013, December). *Application of energy gradient theory in flow instability in a centrifugal pump*. IOP Conference Series: Materials Science and Engineering (Vol. 52, No. 1, p. 012007). IOP Publishing. https://doi.org/10.1088/1757-899x/52/1/012007

Dou, H. S., & Phan-Thien, N. (2007). Viscoelastic flow past a confined cylinder: Instability and velocity inflection. *Chemical Engineering Science*, *62*(15), 3909-3929. https://doi.org/10.1016/j.ces.2007.03.040

Dou, H. S., Khoo, B. C., & Yeo, K. S. (2008). Instability of Taylor–Couette flow between concentric rotating cylinders. *International Journal of Thermal Sciences*, *47*(11), 1422-1435. https://doi.org/10.1016/j.ijthermalsci.2007.12.012

Gao, W., Wei, M., & Huang, S. (2024). Optimization of aerodynamic drag reduction for vehicles with non-smooth surfaces and research on aerodynamic characteristics under crosswind. *Proceedings of the Institution of Mechanical Engineers, Part D: Journal of Automobile Engineering*, *238*(9), 2504-2522. https://doi.org/10.1007/s11771-015-2934-7

Gleason, M. E., Duncan, B., Walter, J., Guzman, A., & Cho, Y. C. (2015). Comparison of computational simulation of automotive spinning wheel flow field with full width moving belt wind tunnel results. *SAE International Journal of Passenger Cars-Mechanical Systems*, *8*(2015-01-1556), 275-293. https://doi.org/10.4271/2015-01-1556

Hucho, W. H. (Ed.). (2013). Aerodynamics of road vehicles: from fluid mechanics to vehicle engineering. *Elsevier*. https://www.yanfabu.com/resources/editupload/files/20131122164618 20.pdf

Huminic, A., & Huminic, G. (2017). Aerodynamic study of a generic car model with wheels and underbody

diffuser. *International Journal of Automotive Technology*, *18*(3), 397-404. https://doi.org/10.1007/s12239-017-0040-6

Jermy, M., Moore, J., & Bloomfield, M. (2008). Translational and rotational aerodynamic drag of composite construction bicycle wheels. *Proceedings of the Institution of Mechanical Engineers, Part P: Journal of Sports Engineering and Technology*, *222*(2), 91-102. https://doi.org/10.1243/17543371jset17

Jiao, D. Q., Huang, T. H., & Zhou, H. C. (2023). *Study on the effects of the spoke surface structures on the aerodynamic characteristics of isolated wheel*. Academic Annual Conference of Automotive, 133-147. https://doi.org/10.26914/c.cnkihy.2023.033227

Josefsson, E., Hobeika, T., & Sebben, S. (2022). Evaluation of wind tunnel interference on numerical prediction of wheel aerodynamics. *Journal of Wind Engineering and Industrial Aerodynamics*, *224*, 104945. https://doi.org/10.1016/j.jweia.2022.104945

Khalighi, B., Zhang, S., Koromilas, C., Balkanyi, S. R., Bernal, L. P., Iaccarino, G., & Moin, P. (2001). Experimental and computational study of unsteady wake flow behind a bluff body with a drag reduction device. *SAE Transactions*, 1209-1222. https://www.jstor.org/stable/44730974

Klingbeil, M., Weissert, J., & Yilmaz, Z. (2016, April). *The new Porsche 911 Carrera–Evolution in aerodynamics, thermal management and heat protection*. 16 Internationales Stuttgarter Symposium: Automobil-und Motorentechnik (pp. 315-330). Wiesbaden:Springer Fachmedien Wiesbaden. https://doi.org/10.1007/978-3-658-13255-2_24

Koppa Shivanna, N., Ranjan, P., & Clement, S. (2021). The effect of rear cavity modifications on the drag and flow field topology of a square back Ahmed body. *Proceedings of the Institution of Mechanical Engineers, Part D: Journal of Automobile Engineering*, *235*(7), 1849-1863. https://doi.org/10.1177/0954407021990918

Li, K., Chen, X., Dou, H. S., Zhu, Z., Zheng, L., & Luo, X. (2019). Study of flow instability in a miniature centrifugal pump based on energy gradient method. *Journal of Applied Fluid Mechanics*, *12*(3), 701-713. https://doi.org/10.29252/JAFM.12.03.28662

Nath, D. S., Pujari, P. C., Jain, A., & Rastogi, V. (2021). Drag reduction by application of aerodynamic devices in a race car. *Advances in Aerodynamics*, *3*(1), 1-20. https://doi.org/10.1186/s42774-020-00054-7

Phan, T. L., Pham, Q. T., Nguyen, T. K. L., & Nguyen, T. T. (2022). A Numerical analysis of active flow control techniques for aerodynamic drag reduction in the square-back ahmed model. *Applied Sciences*, *13*(1), 239. https://doi.org/10.3390/app13010239

Ren, N., Wang, Y., & Trouvé, A. (2013). Large eddy simulation of vertical turbulent wall fires. *Procedia engineering*, *62*, 443-452. https://doi.org/10.1016/j.proeng.2013.08.086

Rong, L., & Yiwan, W. (2019, May). *Effects of riblet shape of non-smooth surface on aerodynamic characteristics of vehicle.* IOP Conference Series: Materials Science and Engineering (Vol. 538, No. 1, p. 012070). IOP Publishing. https://doi.org/10.1088/1757-899X/538/1/012070

Su, X., He, K., Xu, K., Gao, G., & Krajnović, S. (2023). Comparison of flow characteristics behind squareback bluff-bodies with and without wheels. *Physics of Fluids*, 35(3). https://doi.org/10.1063/5.0138305

Viswanath, P. R. (2002). Aircraft viscous drag reduction using riblets. *Progress in Aerospace Sciences*, *38*(6-7), 571-600. https://doi.org/10.1016/s0376-0421(02)00048-9

Wager, G., Whale, J., & Braunl, T. (2016). Driving electric vehicles at highway speeds: The effect of higher driving speeds on energy consumption and driving range for electric vehicles in Australia. *Renewable and sustainable energy reviews*, 63, 158-165. https://doi.org/10.1016/j.rser.2016.05.060

Wang, F., Yin, Z., Yan, S., Zhan, J., Friz, H., Li, B., & Xie, W. (2017a). Validation of aerodynamic simulation and wind tunnel test of the New Buick Excelle GT. *SAE International Journal of Passenger Cars-Mechanical Systems*, *10*(2017-01-1512), 195-202. https://doi.org/10.4271/2017-01-1512

Wang, Y., Wu, C., Tan, G., & Deng, Y. (2017b). Reduction in the aerodynamic drag around a generic vehicle by using a non-smooth surface. *Proceedings of the Institution of Mechanical Engineers, Part D: Journal of Automobile Engineering*, *231*(1), 130-144. https://doi.org/10.1177/0954407016636970

Wickern, G., Zwicker, K., & Pfadenhauer, M. (1997). Rotating wheels-their impact on wind tunnel test techniques and on vehicle drag results. *SAE Transactions*, *106*(6) 254-270. https://www.jstor.org/stable/44731181

Wolf, T. (2020). The aerodynamic development of the new Porsche Cayenne. *Proceedings of the Institution of Mechanical Engineers, Part D: Journal of Automobile Engineering*, *234*(2-3), 390-408. https://doi.org/10.1177/0954407019843004

Xiao, M., Xiao, Q., Dou, H. S., Ma, X., Chen, Y., He, H., & Ye, X. (2016). Study of flow instability in a centrifugal fan based on energy gradient theory. *Journal of Mechanical Science and Technology*, *30*(2), 507-517. https://doi.org/10.1007/s12206-016-0103-z

Yang, Y., Zheng, M., Huang, J., & Nie, Y. (2016). Aerodynamic drag reduction method of vehicle body based on non-smooth surface and vortex interference. *China Mechanical Engineering*, *27*(07), 982.

http://www.cmemo.org.cn/EN/Y2016/V27/I07/982

Zhou, H. C., Wang, G. L., Yang. J., & Xue, K. X. (2015). Numerical Simulation of the Effect of Bionic V-riblet Non-smooth Surface on Tire Anti-hydroplaning. *Journal of Central South University*, *22*, 3900-3908. https://doi.org/10.1007/s11771-015-2934-7

Zhou, H., Qin, R., Wang, G., Xin, L., Wang, Q., & Zheng, Z. (2024). Comparative analysis of the aerodynamic behavior on Ahmed body mounted with different wheel configurations. *Proceedings of the Institution of Mechanical Engineers, Part D: Journal of Automobile Engineering*, *238*(1), 128-146. https://doi.org/10.1177/09544070221121877

Zhou, H. C., Chen, Q. Y., Li, H. Y., & Qin, R. Z. (2022). Reseac-h on passive drag reduction method considering wake structure of an ahmed vehicle. *Journal of Chongqing University of Technology (Natural Science)*, *36*(4), 28 – 34. http://clgzk.qks.cqut.edu.cn/CN/Y2022/V36/I4/28